Original Article

Exploring the optical, structural, morphological and compositional properties of electrosynthesized FeSe/CrSe superlattice thin films

Ifunanya Peace Muogbo [1], Azubike Josiah Ekpunobi [2] (iD), Nonso Livinus Okoli [3]**(iD)

[1] *Department of Physics, Federal College of Education (Technical) Umunze, Nigeria*
[2] *Department of Industrial Physics, Nnamdi Azikiwe University, Awka, Nigeria*
[3] *Madonna University Nigeria, Okija Campus, Nigeria*

ARTICLE INFORMATION

ABSTRACT

Iron selenide/chromium selenide (FeSe/CrSe) superlattice thin films were successfully deposited on conducting substrates (fluorine doped tin oxide) by electrodeposition. The thicknesses of the FeSe/CrSe superlattice thin films were found to range from 125.65 nm to 251.31 nm. The optical properties of the deposited superlattice thin films showed that the absorbance ranged from 11.70% to 80.91% and the transmittance values ranged from 15.52% to 76.39%. These films showed low reflectance values in all the wavelength regions studied, with the maximum reflectance values within the UV region. The refractive indices of deposited thin films ranged from 2.03 to 2.62. The extinction coefficient of the films ranged from 1.20 to 3.09. The energy bandgap values of the films vary with the deposition potential, from 2.60 to 3.10 eV. The structural analysis of these films confirmed that FeSe/CrSe superlattice thin films exhibited peaks corresponding to the hexagonal structural phases of these binary compounds. Average crystallite sizes were found to range from 18.844 nm to 40.766 nm. The dislocation density of the films ranged from 1.871 to 3.597 lines/m^2 while the microstrain ranged from 4.120 to 6.073. The structural results showed that crystallite size of the films increased as deposition potential increased, while dislocation density and microstrain of the films were found to decrease with an increase in deposition potentials. SEM images revealed that the surfaces are made up of tiny, agglomerated particles of different sizes and shapes. Analyses of EDS spectra showed that these films are made up of desired elements.

Corresponding author, email: okolinonsolivinus@gmail.com (N.L. Okoli), muogboifunanya@gmail.com (I. P. Muogbo)

Graphical Abstract
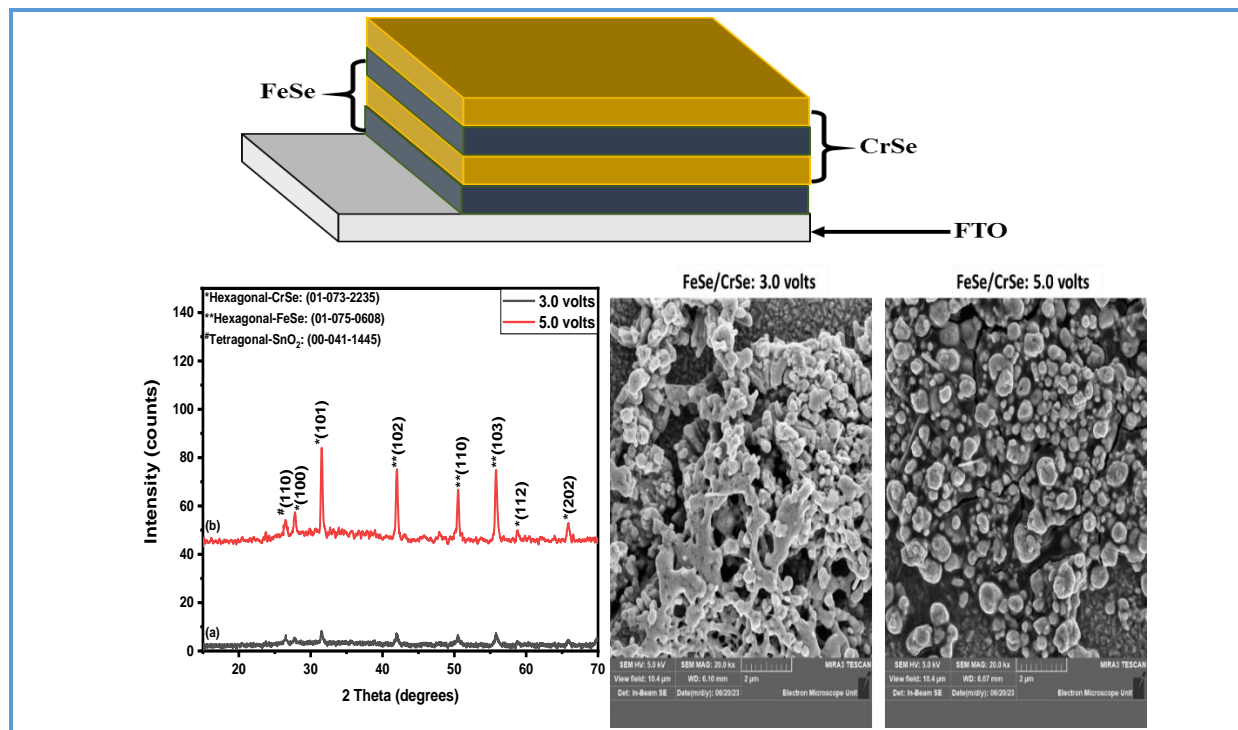
Introduction

In the field of materials science and nanotechnology, the exploration of novel thin film materials has grown rapidly in recent years, driven by the promise of tailored electronic, optical, and structural properties for a multitude of applications such as in solar cells [1-5], gas sensing [6-9], and supercapacitors [10-13]. Among these emerging materials, superlattice thin films have garnered considerable attention due to their unique and tunable characteristics. A superlattice (SL) is a structure where two different materials are grown to a specific thickness in alternating layers [14]. Superlattice structures have exceptional electronic properties that are not present in bulk materials. Studying these properties can provide insights into the underlying properties of superlattice structures that make them

suitable materials for design of next-generation electronic and optoelectronic devices.

In recent years, iron selenide (FeSe) has gained significant attention as a semiconducting thin film material due to its intriguing electronic properties, including tunable bandgap, excellent charge carrier mobility, and compatibility with various substrates [15-17]. FeSe primarily demonstrates two crystalline structures: a tetragonal phase and a hexagonal phase [18]. [19] investigated how deposition potential influences the properties of electrochemically grown iron selenide thin films, revealing a hexagonal wurtzite structure with well-defined morphology. The films demonstrated an energy band gap ranging from 1.19 to 1.21 eV and magnetic properties, including coercivity (255 Oe), remanence (39 emu/cc), and saturation magnetization (300 emu/cc). [20] studied the thickness, structure, composition, and optical properties of electrochemically

grown iron selenide and iron diselenide thin films. The magnetic semiconductors showed an energy gap value between 1.23 and 1.08 eV.

Chromium selenide (CrSe) thin films have garnered significant attention in recent years due to their intriguing electronic, optical, and magnetic properties [21-22]. These films exhibit a range of distinctive properties, including semiconducting behavior, magnetic ordering, and a wealth of potential applications in fields such as spintronics, photodetectors, and catalysis. [8] synthesized chromium selenide (CrSe) thin films on commercial glass substrates. Optical band gap ranging from 3.80 to 3.92 eV, film thickness changing between 76 nm and 126 nm for different pH levels. These results highlight the pH effectiveness in tailoring the properties of CrSe thin films.

The synthesis of high-quality FeSe and CrSe thin films is a critical aspect of harnessing their semiconducting properties. Several methods have been employed to synthesize FeSe and CrSe thin films which include electrodeposition [20,23-24], chemical vapor deposition [25-26], molecular beam epitaxy [22], and pulsed laser deposition [27-28], electron beam evaporation [17] and chemical bath method [21,29-31]. These methods have enabled researchers to explore the growth mechanisms and optimize the synthesis process.

Electrochemical deposition, also known as electrodeposition or electrosynthesis, is a straightforward and adaptable chemical solution deposition technique reliant on redox reactions occurring within an electrochemical cell [18,32]. The electrochemical cell comprises a container housing an electrolytic bath with a working electrode, a counter electrode, and a reference electrode, as shown in Figure 1. The reference electrode is essential as it furnishes a stable ground voltage necessary for precise measurement of electrochemical potentials [18]. This is achieved by ensuring an isolated and stable chemical reaction that generates a known voltage. The reference electrode is positioned in close proximity to the working electrode to determine its potential in relation to the stable reference electrode. In real-world applications, thin films of binary and ternary compounds are deposited using user-friendly reference electrodes such as saturated calomel (Hg_2Cl_2) or silver chloride (Ag/AgCl). In this type of reference electrodes, electron and ion transfers take place at the electrodes' surfaces as a result of chemical reactions that are ideally controlled by the electrode voltage. The working electrode usually acts as a substrate, and the voltage and current between the electrodes control the chemical reactions.

In this work, the study delves into the intricate world of superlattice thin films with a focus on the electrosynthesis and comprehensive characterization of FeSe/CrSe superlattice thin films. Iron selenide (FeSe) and chromium selenide (CrSe), both with their distinct electronic and magnetic properties, have been combined in a superlattice structure using an electrodeposition approach on fluorine-doped tin oxide (FTO) as conducting substrates. This choice of materials and synthesis method opens up a captivating avenue for engineering multifunctional thin films with tailored properties.

Materials and methods

Reagents

Reagents used for electrodeposition of iron selenide/chromium selenide (FeSe/CrSe) were iron (II) tetraoxosulphate (VI) as precursor for iron ion, chromium (III) and trioxonitrate (V) nanohydrate as precursor for chromium ion, selenium (IV) oxide as precursor for selenium ion, sodium sulphate as supporting electrolyte and distilled water was used as solvent.

Apparatus

Apparatus used during the experiment include; beakers (l00 mI): used for mixing solutions, fluorine doped tin oxide (FTO) glass slide (17 Ω/sq): this is used as the substrates or working electrode, electronic compact scale (Atom: model 110C, capacity – 750 g, accuracy - 0.01 g): used for the determination of the weight of reagents, magnetic stirrer hotplate (Labscience 85 – 2): used for stirring the solutions, DC Power Supply: served as a source of electric energy (potential difference) Digital multimeters (DT9201A CE and Mastech: MY60): for measuring current and potential difference, platinum rod: used as counter electrode, Ag/AgCl electrode: used as reference electrode, ultrasonic bath: for degreasing the substrates and electrical oven used for drying.

Material preparation

The reagents are of analytical grade and used without further purification or modification. The desired molar solutions of the reagents were prepared and used for the depositions. 0.10 M of iron (II) tetraoxosulphate (VI) heptahydrate salt was prepared by dissolving 6.95 g in 250 ml of distilled water. 0.10 M of chromium (III) trioxonitrate (V) nanohydrate was prepared by dissolving 10.00 g of the compound in 250 ml of distilled water. 0.10 M of SeO_2 was prepared by dissolving 2.77 g in 250 ml of distilled water. 0.05 M of sodium sulphate (Na_2SO_4) which was used as supporting electrolyte was prepared by dissolving 8.06 g in 500 ml of double distilled water.

Substrate pre-treatment

The cleaning process for preparing FTO (Fluorine-doped Tin Oxide) glass substrates for electrodeposition of films involves several crucial steps. Initially, the FTO glass slides are meticulously cleaned with a detergent solution to eliminate any surface dust, dirt, or contaminants that could hinder the subsequent stages of preparation. Following this, the slides are immersed in acetone for a period of 10 minutes to effectively degrease the surface, removing any residual oils or greases that might interfere with film adhesion. Subsequently, the substrates undergo ultrasonic treatment in an ultrasonic bath for 10 minutes.

This step employs high-frequency vibrations to dislodge and eliminate any remaining particles or contaminants adhering to the substrate. Finally, to ensure complete dryness, the substrates are placed in an electric oven and heated to 100 °C for 10 minutes, ensuring the removal of any lingering moisture that could negatively affect the electrodeposition process and the films adhesion.

Electrodepostion of FeSe/CrSe superlattice thin films

Figure 1 depicts the electrodeposition setup, which includes the electrolyte, power supply unit, and the electrodes. The electrodeposition setup utilized in this work is identical to the one employed by [33], as illustrated in Figure 1. The setup consisted of a three-electrode electrodeposition configuration for deposition of thin films on a conducting substrate. The conducting substrate, FTO (Fluorine-doped Tin Oxide) glass, served as the working electrode, functioning as the cathode. A platinum electrode was employed as the counter electrode which served as the anode. An Ag/AgCl electrode was utilized as the reference electrode. The Dazheng digital DC-power supply unit (PS-1502A) model served as the

energy source for the electrodeposition setup. Two digital multimeters (DT9201A CE, and Mastech MY60) were incorporated into the setup to measure potential difference and current, respectively.

To initiate the electrodeposition of iron selenide (FeSe) thin films onto an FTO substrate, a well-mixed aqueous electrolytic bath was formulated. This bath comprised 15 ml of 0.10 M iron (II) tetraoxosulphate (VI) and 15 ml of 0.10 M selenium dioxide, properly mixed using a magnetic stirrer for 5 minutes to form a homogenous mixture. Following this, 5 ml of 0.05 M Na_2SO_4 was introduced, and the resulting solution underwent an additional 5 minutes of magnetic stirring. Subsequently, the three electrodes were immersed into the electrolytic bath, and a consistent potential of 3.0 volts was constantly maintained for precisely 2 minutes. This controlled electrochemical process culminated in the formation of FeSe thin film deposit, which was subsequently subjected to a thermal treatment at 100 °C for a duration of 20 minutes to optimize its properties.

Continuing on the same substrate, chromium selenide (CrSe) thin films were deposited using a separate aqueous electrolytic bath. This bath consisted of 15 ml of 0.20 M chromium (III) trioxonitrate (V) nanohydrate and 15 ml of 0.10 M selenium dioxide, mixed thoroughly with magnetic stirrer for 5 minutes.

Following this, 5 ml of 0.05 M Na_2SO_4 was introduced, and the final solution underwent an additional 5 minutes of magnetic stirring. The three electrodes were then carefully immersed in the electrolytic bath, and a stable potential of 3.0 volts was carefully maintained for exactly 2 minutes. This precisely controlled electrochemical process led to the formation of a distinct FeSe/CrSe superlattice structure.

This procedure was iteratively conducted to fabricate four alternative layers of FeSe and CrSe on the same substrate, as illustrated in Figure 2.

Furthermore, to explore the effect of different potentials on the deposited superlattice, four additional FeSe/CrSe superlattice structures were precisely formed at varying potentials of 3.5 volts, 4.0 volts, 4.5 volts, and 5.0 volts.

Characterization of deposited superlattice

The electrosynthesized FeSe/CrSe thin films were subjected to optical, morphological, compositional and structural studies. Optical study was carried out using 756S UV-VIS spectrophotometer. Morphology and compositional analysis were carried out using Nova NanoSEM and MIRA TESCAN SEM machine while structural analysis of the films were obtained using Drawell x-ray diffractometer.
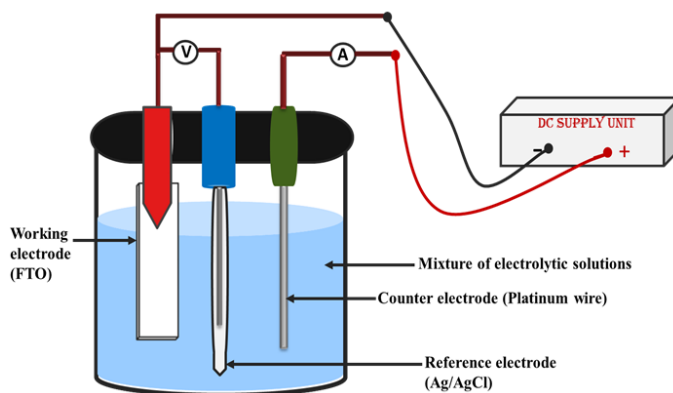

Figure 1. Schematic diagram of the electrodeposition experimental setup [33].

Figure 2. Diagrammatical representation of FeSe/CrSe superlattice formed by electrodeposition.

Results and Discussion

Optical properties of FeSe/CrSe superlattice thin films

Absorbance values of the films were measured with UV-VIS spectrophotometer within the wavelength of 300 nm to 1100 nm. Other properties such as transmittances, reflectance, refractive index, extinction coefficient, and energy band gap were evaluated according to expressions as described below. Transmittance of the film was evaluated using Equation (1) as given by [34-35].

$$T = 10^{-A} \tag{1}$$

Reflectance was obtained using the expression in equation (2) as given by [33,36].

$$R = 1 - [T \cdot \exp(A)]^{\frac{1}{2}} \tag{2}$$

The absorption coefficient (α) was calculated from the transmittance values using Equation (3) as given by [37-38].

$$\alpha = \frac{1}{t} \ln\left(\frac{1}{T}\right). \tag{3}$$

Where, t is film thickness obtained using gravimetric method as described by [37, 39-40].

Extinction coefficient was obtained using equation (4) as given by [41-42].

$$k = \frac{\alpha \lambda}{4\pi} \tag{4}$$

Refractive indices of the films were calculated using Equation (5) as given by [43-44]:

$$\eta = \frac{1+R}{1-R} + \sqrt{\frac{4R}{(1-R)^2} - k^2} \tag{5}$$

The energy band gap was estimated using Tauc's model of equation (6) as given by [45-47]:

$$(\alpha h v)^n = \beta (h v - E_g) \tag{6}$$

Where, β is a constant, $n = 2$ for direct band gap. The energy band gaps of the films were obtained by extrapolating the straight portion of the plot of $(\alpha h v)^2$ against the photon energy $(h v)$ at $(\alpha h v)^2 = 0$.

Figure 3 displays the absorbance graph plotted against wavelength for FeSe/CrSe thin films electrodeposited at various deposition potentials. The results reveal a consistent trend of decreasing absorbance as photon wavelength increases. Interestingly, superlattice films demonstrate an inverse correlation between absorbance and deposition potential, with the 5.0-volt deposition registering the highest absorbance at 80.91% at 300 nm.

In contrast, the 3.0-volt thin film exhibits a decline in absorbance from 27.60% at 300 nm to 20.57% at 400 nm, followed by a further decrease to 12.11% at 700 nm and 11.70% at 1000 nm in the near-infrared (NIR) range. A similar pattern is observed for films deposited at 3.5, 4.0, and 4.5 volts, with decreasing absorbance as wavelength increases, indicating the critical role of deposition potential in tailoring absorbance characteristics for specific applications.

Due to the high absorbing nature of these films within UV region, they could be used in antireflective window coating in tropical regions of the world to shield harmful effect of UV radiations. Similar trend of increase in absorbance as deposition potential increases was obtained by [48].

Figure 4 shows the graph of transmittance plotted against wavelength for FeSe/CrSe thin films deposited at different deposited potential. Transmittance values increase with longer wavelengths, while they decrease as the deposition potential rises. This reduction in

transmittance at higher deposition potentials results from increased photon energy absorption due to thicker films. For instance, the 3.0-volt deposition yields transmittance values rising from 52.97% at 300 nm to 62.27% at 400 nm, and further to 75.67% at 700 nm, and 76.39% at 1000 nm. Similarly, the 3.5-volt film exhibits transmittance values increasing from 31.15% at 300 nm to 40.59% at 400 nm, with enhancements to 63.73% at 700 nm and 71.31% at 1000 nm. The 4.0-volt deposition results in transmittance values
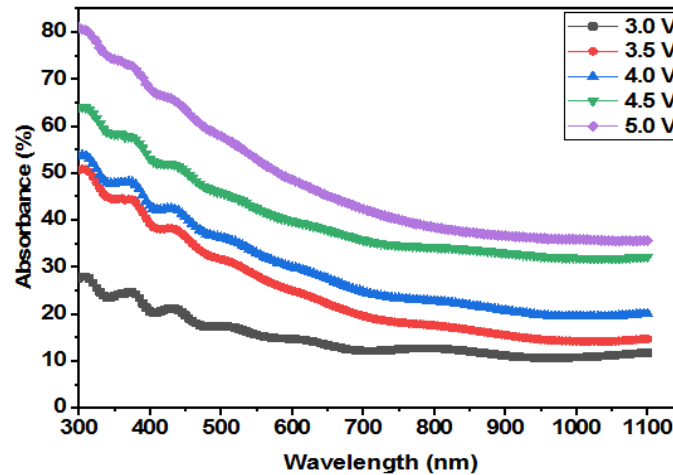

Figure 3. Plot of absorbance against wavelength for FeSe/CrSe superlattice thin films deposited at different deposition potential.
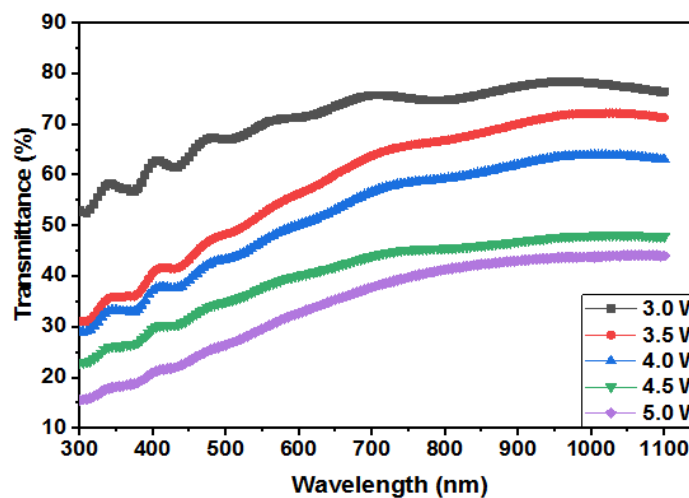

Figure 4. Plot of transmittance against wavelength for FeSe/CrSe superlattice thin films deposited at different deposition potential.

escalating from 29.08% at 300 nm to 45.60% at 400 nm and further to 37.12% at 700 nm, and 56.61% at 1000 nm. Lastly, the 4.5-volt deposition leads to transmittance values increasing from 22.93% at 300 nm to 29.50% at 400 nm, further enhancing to 43.94% at 700 nm, and up to 47.75% at 1000 nm. This trend aligns with previous reports by [49-50] regarding decreased transmittance with increasing applied potential.

Figure 5 shows the graph of reflectance plotted against wavelength for FeSe/CrSe thin films deposited at different values of deposition potential. The results shows that reflectance values generally remained low, decreasing at 3.0 volts as wavelength

increased. Also, gradual increase at 3.5 volts and 4.0 volts was observed within UV and VIS regions, and remaining constant in the NIR region, while at 4.5 volts and 5.0 volts, reflectance increased with wavelength within UV and VIS regions, and the reflectance values did not exhibit a linear trend with deposition potential in the UV and VIS regions, but increased with deposition potential in the NIR region.

Figure 6 demonstrates the graph of refractive index plotted against wavelength for FeSe/CrSe thin films deposited at different values of deposition potential. Refractive index values of deposited FeSe/CrSe were found to
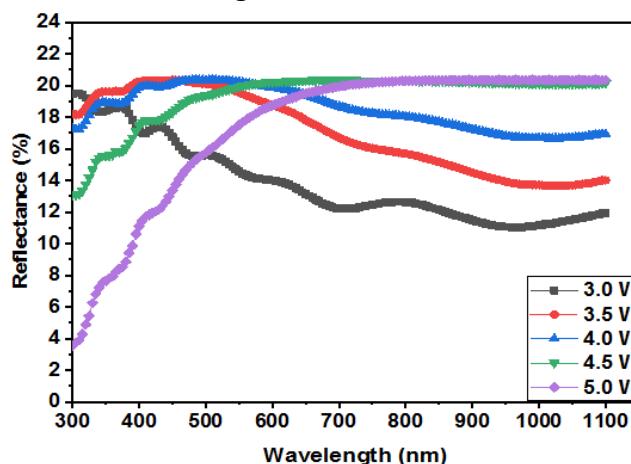

Figure 5. Plot of reflectance against wavelength for FeSe/CrSe superlattice thin films deposited at different deposition potential.
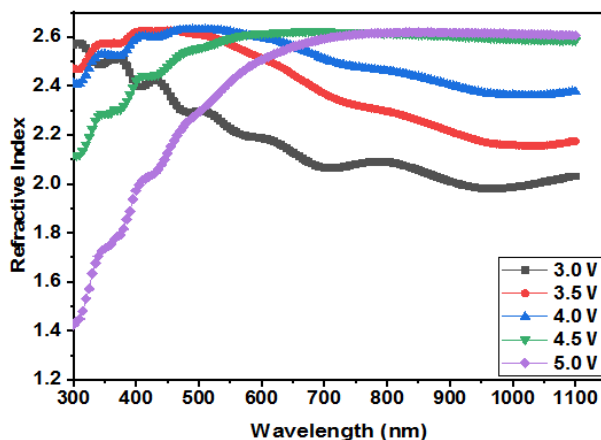

Figure 6. Plot of refractive index against wavelength for FeSe/CrSe superlattice thin films deposited at different deposition potential.

be low. From the graph, the refractive index decreases with increasing wavelength for the film deposited at 3.0 volts, while films deposited at 3.5 volts and 4.0 volts display a gradual increase within the 300 nm to 450 mm wavelength range, followed by a decrease beyond 450 nm. Conversely, films deposited at 4.5 volts and 5.0 volts exhibit increasing refractive index values within the UV and VIS regions, remaining stable in the NIR region. Interestingly, the refractive index values do not exhibit a linear correlation with deposition potential in the UV and VIS regions, but do show an increase with higher deposition potentials in the NIR region. The refractive index values of the 3.0-volt film range between 2.57 and 2.03, while those of the 3.5-volt film span from 2.47 to 2.17. The 4.0-volt deposition results in values between 2.41 and 2.38, with the 4.5-volt deposition yielding values from 2.12 to 2.59. Finally, the 5.0-volt deposition produces values ranging from 1.42 to 2.61.

Figure 7 illustrates the graph of extinction coefficient of FeSe/CrSe thin films at varying deposition potential. Extinction coefficient values of the films were found to increase as wavelength increases except for film deposited at potential of 3.5 volts that showed a different trend in the extinction coefficient. Furthermore, no linear relationship was observed between deposition potential and extinction coefficient of the deposited FeSe/CrSe thin films.

FeSe/CrSe thin films deposited at 3.0 volts, 3.5 volts, 4.0 volts, 4.5 volts and 5.0 volts have extinction coefficient values that ranged from 1.21×10^{-1}-1.88×10^{-1}, 1.81×10^{-1}-$1.1.93 \times 10^{-1}$, 1.51×10^{-1}-2.07×10^{-1}, 1.68×10^{-1}-3.09×10^{-1}, and 1.77×10^{-1}-2.86×10^{-1}, respectively. These range of extinction coefficient values confirmed these films are good for absorber layer of thin film solar cells.

Figure 8 shows the plot of $(\alpha h v)^2$ against photon energy for FeSe/CrSe thin films deposited at different deposition potentials. From the plot, energy band gap of the films were estimated by extrapolation of the straight portion of the graph along the photon energy axis, where $(\alpha h v)^2 = 0$. Energy band gap of 3.10 eV was obtained for FeSe/CrSe thin film deposited at 3.0 volts while band gap values of 3.00 eV, 2.80 eV, 2.70 eV, and 2.60 eV were obtained for FeSe/CrSe thin films deposited at 3.5 volts, 4.0 volts, 4.5 volts, and 5.0 volts, respectively.
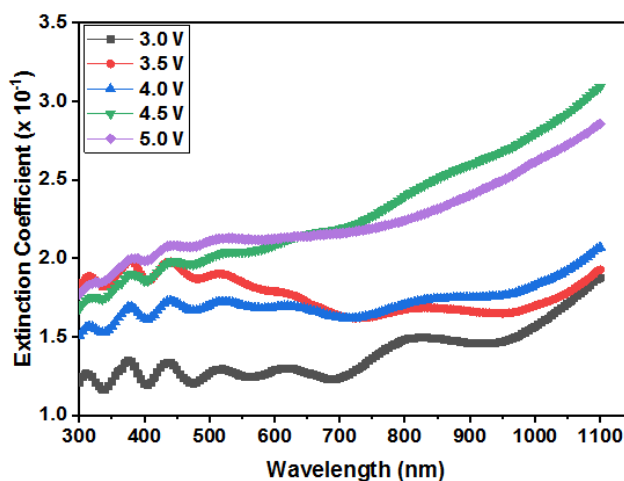

Figure 7. Plot of extinction coefficient against wavelength for FeSe/CrSe superlattice thin films deposited at different deposition potential.
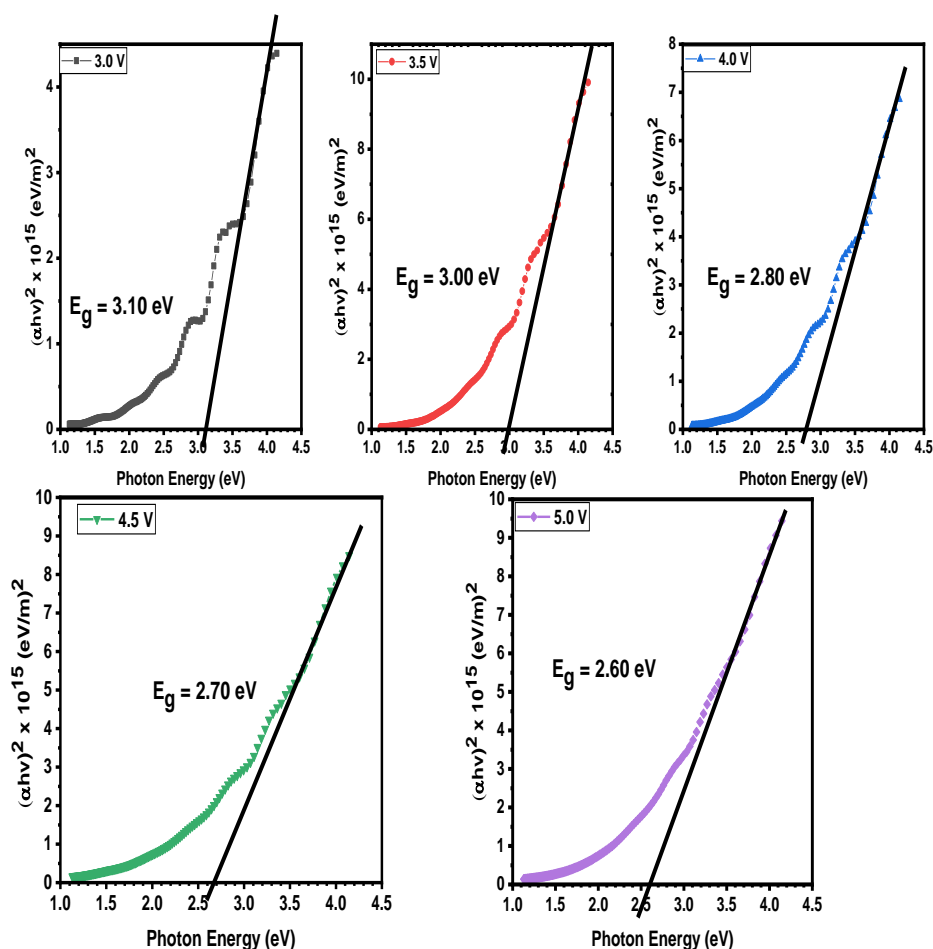
Figure 8. Plot of $(\alpha h v)^2$ against photon energy for FeSe/CrSe superlattice thin films deposited at different deposition potential.

The result showed a decrease in energy band gap of films as deposition potential increases. This confirmed the likelihood of tuning energy band gap of FeSe/CrSe by varying the deposition potential. Similar effect of deposition potential on the band gap of thin film materials had been reported by [49-50]. The increase in deposition potential gives rise to increase in the films thickness which is likely to be due to quantum confinement effect.

Morphological study of FeSe/CrSe superlattice thin films

Figure 9 displays SEM images of FeSe/CrSe superlattice thin films deposited at deposition potentials of 3.0 volts and 5.0 volts. These images reveal agglomerated nanoparticles of varying sizes and shapes on the film surfaces, with greater particle agglomeration at higher deposition potentials. Notably, the SEM image of film deposited at potential of 3.0 volts shows interconnected nanoparticles while SEM image of superlattice film deposited at potential of 5.0 volts exhibits aggregated particles. Quantitative analysis confirms that the average particle size increases from 52.87 nm to 80.16 nm as the deposition potential rises from 3.0 to 5.0 volts. This underscores the direct impact of deposition potentials on particle behavior and film morphology.
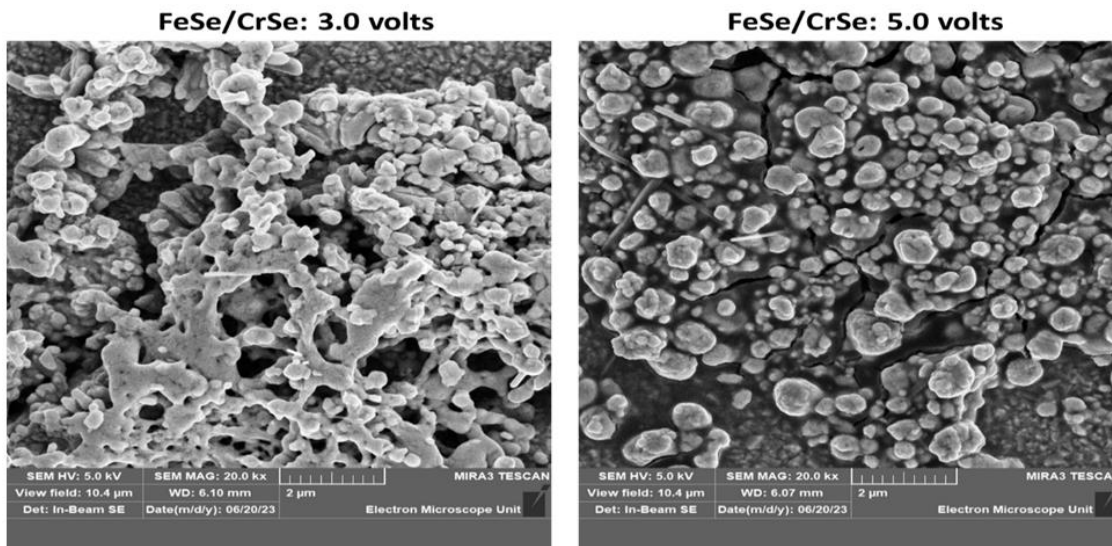
Figure 9. SEM image of FeSe/CrSe thin films deposited at 3.0 volts and 5.0 volts.

The findings emphasize the intricate interplay between electrochemical factors and surface characteristics in FeSe/CrSe superlattice thin films. This relationship holds significance for tailoring thin films for specific applications.

Compositional study of FeSe/CrSe superlattice thin films

Figure 10 shows the EDS spectrum of FeSe/CrSe thin film deposited at 3.0 and 5.0 volts. The EDS spectrum confirmed the presence of iron (Fe), chromium (Cr), and selenium (Se). Other elements such as oxygen (O), carbon (C), silicon (Si), and tin (Sn) were found to be presence in the sample. These elements are attributed to elemental composition of the substrate used for the deposition. Atomic percentage of iron and chromium were found to increase slightly as deposition potential increased from 3.0 volts to 5.0 volts while atomic percentage of Se was found to decrease as deposition potential increased from 3.0 volts to 5.0 volts.
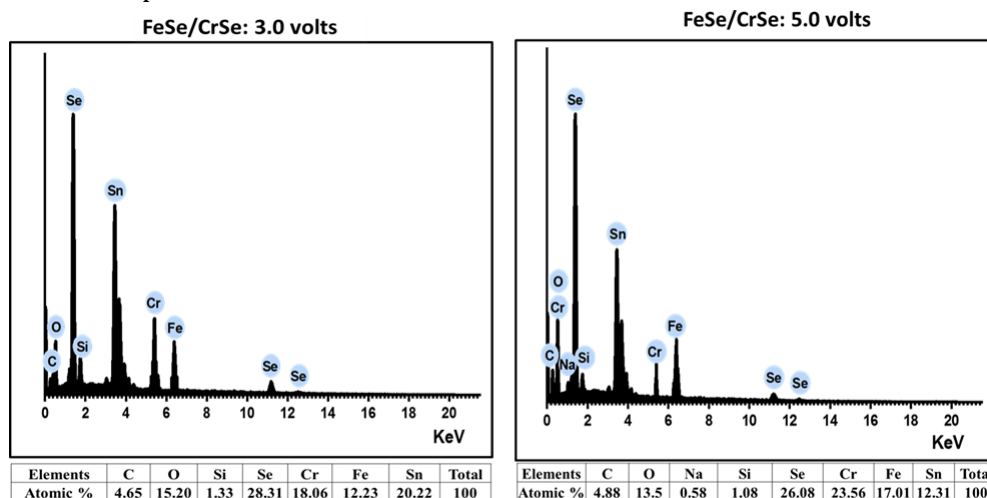

Elements	C	O	Si	Se	Cr	Fe	Sn	Total
Atomic %	4.65	15.20	1.33	28.31	18.06	12.23	20.22	100

Elements	C	O	Na	Si	Se	Cr	Fe	Sn	Total
Atomic %	4.88	13.5	0.58	1.08	26.08	23.56	17.01	12.31	100

Figure 10. EDS spectrum of FeSe/CrSe thin films deposited at 3.0 volts and 5.0 volts.

Structural analysis of FeSe/CrSe superlattice thin films

Figure 11 shows the x-ray diffraction pattern of electrodeposited FeSe/CrSe superlattice thin films deposited at deposition potential of 3.0 and 5.0 volts. The result shows that the fabricated FeSe/CrSe superlattice thin films have mixed hexagonal structural phases of FeSe and CrSe belonging to the JCPDS file numbers (01-075-0608) and (01-073-2235). Peaks corresponding to peaks of these standard JCPDS file were observed for the superlattice films.

FeSe/CrSe superlattice thin film deposited at 3.0 volts showed 6 peaks of which three peaks at 27.537°, 31.548° and 65.876° belong to hexagonal CrSe while the remaining three peaks at 42.001°, 50.500° and 55.848° belong to hexagonal FeSe. FeSe/CrSe superlattice thin film deposited at 5.0 volts showed 7 peaks of which four peaks at 27.839°, 31.539°, 58.949°, and 66.015° belong to hexagonal CrSe while the remaining three peaks at 42.000°, 50.521°, and 55.822° belong to hexagonal FeSe.

One additional peak at 26.504° was observed which belong to SnO_2. The intensity of diffraction spectra were found to increase as deposition potential increases. The crystallite sizes of the films were evaluated using Scherrer's formula. Debye-Scherrer's formula for calculating crystallite sizes of a thin film material as given by [51-53] in Equation (7):

$$D = \frac{0.9\,\lambda}{\beta\cos\theta}. \qquad (7)$$

The dislocation density (δ) of thin films can be estimated using expression as provided by [54-56] in Equation (8).

$$\delta = \frac{1}{D^2}. \qquad (8)$$

Micro-strain (ε) of thin film sample can be estimated using the expression in Equation (9) as given by [57-58].

$$\varepsilon = \frac{\beta}{4\tan\theta} \qquad (9)$$

Table 1 shows the structural parameters of the deposited FeSe/CrSe thin films. In all the thin film samples, preferential orientation was observed at (101) plane for CrSe and (103) for FeSe structural phases.
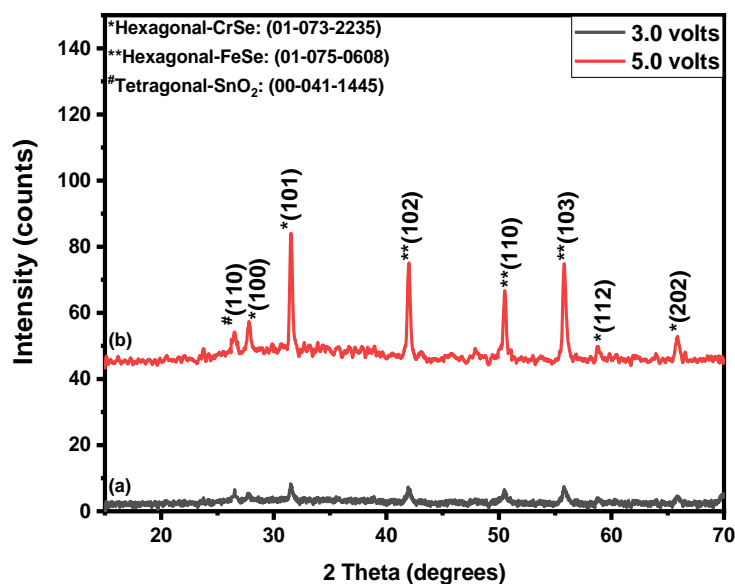

Figure 11. X-ray spectra of FeSe/CrSe thin films deposited at (a) 3.0 volts and (b) 5.0 volts.

Table 1. Crystal structural properties of FeSe/CrSe thin films formed at 3.0 volts and 5.0 volts

Sample	2θ (º) Observed	D – spacing (Å) Observed	[hkl]	FWHM (º)	Crystallite Size (nm)	$\delta \times 10^{15}$ lines/m²	$\varepsilon \times 10^{-3}$
3.0 volts	27.537*	3.235	100	0.718	11.903	7.058	12.774
	31.548*	2.834	101	0.321	26.886	1.383	4.953
	42.001**	2.149	102	0.465	19.099	2.741	5.289
	50.500**	1.806	110	0.681	13.471	5.510	6.300
	55.848**	1.645	103	0.525	17.880	3.128	4.324
	65.876*	1.417	202	0.415	23.827	1.761	2.794
	Average				**18.844**	**3.597**	**6.073**
5.0 volts	27.839*	3.202	100	0.751	11.387	7.712	13.217
	31.539*	2.834	101	0.272	31.684	0.996	4.205
	42.000**	2.149	102	0.318	27.960	1.279	3.613
	50.521**	1.805	110	0.325	28.210	1.257	3.007
	55.822**	1.646	103	0.364	25.762	1.507	3.002
	58.949*	1.566	112	0.100	95.309	0.110	0.772
	66.015*	1.414	202	0.152	65.051	0.236	1.022
	Average				**40.766**	**1.871**	**4.120**

Conclusion

Iron selenide/chromium selenide (FeSe/CrSe) superlattice thin films were successfully electrodeposited onto conducting substrates (FTO: fluorine-doped tin oxide). Extensive analyses encompassing optical, structural, morphological, and compositional aspects were conducted. Absorbance values of the superlattice thin film exhibited an increase with higher deposition potential and a decrease with longer wavelengths. The superlattice film deposited at 3.0 volts exhibited absorbance values of 27.60% at 300 nm, 20.57% at 400 nm, 12.11% at 700 nm, and 11.70% at 1000 nm. In contrast, the thin film deposited at 5.0 volts displayed the highest absorbance, with a value of 80.91% at 300 nm. Transmittance values decreased as deposition potential increased and increased with longer wavelengths. At 3.0 volts, transmittance ranged from 52.97% at 300 nm to 76.39% at 1000 nm, while at 5.0 volts, transmittance values followed a similar trend, emphasizing the wavelength-dependent and potential-dependent behavior of transmittance FeSe/CrSe superlattice thin films.

These films displayed consistently low reflectance values across all studied wavelength regions, with the highest reflectance found in the UV region. Refractive index values decreased with longer wavelengths and increased with higher deposition potentials. No linear relationship was found for the extinction coefficient variation with the number of deposition potentials. Energy bandgap values decreased from 3.10-2.60 eV as deposition potential increased from 3.0 to 5.0 volts. These energy

band gap values indicate that FeSe/CrSe superlattice thin films are wide-bandgap semiconductors suitable for optoelectronic applications. Structural analysis revealed increasing crystallite sizes from 18.844-40.766 nm as deposition potential increases. Dislocation density was found to decrease from 3.597×10^{15} -1.871×10^{15} lines/m^2 while microstrain decreased from 6.073×10^{-3} - 4.120×10^{-3} as deposition potential increases. Surface morphology studies revealed diverse particle sizes and shapes, predominantly tiny agglomerated particles. Elemental analysis confirmed the presence of iron (Fe), chromium (Cr), selenium (Se), and trace elements, likely originating from the substrate composition.

Orcid

Azubike J. Ekpunobi : 0000-0002-5111-7298
Nonso Livinus Okoli : 0000-0003-1411-321X

References

[1]. Kadhim M., Adail Glob M. The Effect of Double Spectrum Colors Factor on Solar Cells Performance in Inorganic Solar Cells, *J. Chem. Rev.*, 2023, **5**:353 [Crossref], [Publisher]

[2]. Lal N., Chawla K., Sharma S., Chouhan R.L., Lal C. *J. Indian Chem. Soc.*, 2023, **100**:101006 [Crossref], [Google Scholar], [Publisher]

[3]. Abel S., Tesfaye J.L., Nagaprasad N., Shanmugam R., Dwarampudi L.P., Deepak T., Zhang H., Krishnaraj R., Stalin B. *Bioinorg. Chem. Appl.*, 2022, **2022**: 1003803 [Crossref], [Google Scholar], [Publisher]

[4]. Alyobi M.M., Alamri S.N. *J. Taibah Univ. Sci.*, 2023, **17**:2271232 [Crossref], [Google Scholar], [Publisher]

[5]. Ben Hjal A., Pezzato L., Colusso E., Alouani K., Dabalà M. *Ionics*, 2023, 1 [Crossref], [Google Scholar], [Publisher]

[6]. Sharma A., Gupta G. *Mater. Sci. Eng. B*, 2023, **290**:116333 [Crossref], [Google Scholar], [Publisher]

[7]. Rzaij J.M., Abass A.M. *J. Chem. Rev*, 2020, **2**:114 [Crossref], [Google Scholar], [Publisher]

[8]. Zheng W., Yang C., Li Z., Xie J., Lou C., Lei G., Liu X., Zhang J. *Sens. Actuators B Chem.*, 2021, **329**:129127 [Crossref], [Google Scholar], [Publisher]

[9]. Liu S., Liu Y., Li H., Bai Y., Xue J., Xu R., Zhang M., Chen G. *Nanotechnol.*, 2022, **33**:215501 [Crossref], [Google Scholar], [Publisher]

[10]. Al-Zohbi F. *J. Chem. Rev.*, 2023, **5**:143 [Crossref], [Google Scholar], [Publisher]

[11]. Khot S., Malavekar D., Nikam R., Ubale S., Bagwade P., Patil D., Lokhande V., Lokhande C. *Synth. Met.*, 2022, **287**:117075 [Crossref], [Google Scholar], [Publisher]

[12]. Scarpa D., Cirillo C., Ponticorvo E., Cirillo C., Attanasio C., Iuliano M., Sarno M. *Mater.*, 2023, **16**:5309 [Crossref], [Google Scholar], [Publisher]

[13]. Abbas Q., Khurshid H., Yoosuf R., Lawrence J., Issa B.A., Abdelkareem M.A., Olabi A.G. *Sci. Rep.*, 2023, **13**:15654. [Crossref], [Google Scholar], [Publisher]

[14]. Kane M.H., Arefin N. *(LEDs)*, *Elsevier*, 2014, 99. [Crossref], [Google Scholar], [Publisher]

[15]. Ubale A.U., Sakhare Y.S., Bhute M.V., Belkhedkar M.R., Singh A. *Solid State Sci.*, 2013, **16**:134 [Crossref], [Google Scholar], [Publisher]

[16]. Qasrawi A.F., Toubasi A.J. *Optik*, 2023, **287**:171173 [Crossref], [Google Scholar], [Publisher]

[17]. NM S.S.B., Chandra Mohan R., Saravana Kumar S., Ayeshamariam A., Jayachandran M. *Fluid Mech Open Acc*, 2017, **4**:6 [Crossref], [Google Scholar], [Publisher]

[18]. Piperno L., Celentano G., Sotgiu G. *Coatings*, 2023, **13**:1905 [Crossref], [Google Scholar], [Publisher]

[19]. Thanikaikarasan S., Perumal R., Marjorie S.R. *J. Alloys Compd.*, 2020, **848**:156348 [Crossref], [Google Scholar], [Publisher]

[20]. Thanikaikarasan S., Perumal R., Thanikaivelan E., Ahamad T., Alshehri S.M. *J. New Mater. Electrochem. Syst.*, 2023, **26**:101 [Crossref], [Google Scholar], [Publisher]

[21]. Kariper I. *J. Non-Oxide Glass.,* 2015, **7**:37 [Google Scholar], [Publisher]

[22]. Roy A., Dey R., Pramanik T., Rai A., Schalip R., Majumder S., Guchhait S., Banerjee S.K. *Phys. Rev. Mater.*, 2020, **4**:025001 [Crossref], [Google Scholar], [Publisher]

[23]. Zeynalova A.O., Javadova S.P., Majidzade V.A., Sh A.A. 2021, 262 [Crossref], [Google Scholar], [Publisher]

[24]. Pesko E., Zukowska G., Zero E., Krzton-Maziopa A. *Thin Solid Films*, 2020, **709**:138121 [Crossref], [Google Scholar], [Publisher]

[25]. Hussain R.A., Badshah A., Younis A., Khan M.D., Akhtar J. *Thin Solid Films*, 2014, **567**:58 [Crossref], [Google Scholar], [Publisher]

[26]. Akhtar M., Malik M.A., Raftery J., O'Brien P. *J. Mater. Chem. A*, 2014, **2**:20612 [Crossref], [Google Scholar], [Publisher]

[27]. Obata Y., Karateev I.A., Pavlov I., Vasiliev A.L., Haindl S. *Micromachines*, 2021, **12**:1224 [Crossref], [Google Scholar], [Publisher]

[28]. Obata Y., Sato M., Kondo Y., Yamaguchi Y., Karateev I.A., Pavlov I., Vasiliev A.L., Haindl S. *ACS Appl. Mater. Interfaces*, 2021, **13**:53162 [Crossref], [Google Scholar], [Publisher]

[29]. Sohrabi P., Ghobadi N. *Appl. Phys. A*, 2019, **125**:1 [Crossref], [Google Scholar], [Publisher]

[30]. Kariper I.A. *Opt. Rev.*, 2017, **24**:139 [Crossref], [Google Scholar], [Publisher]

[31]. Tezel F.M., Kariper İ.A. *MRX*, 2018, **6**:036412 [Crossref], [Google Scholar], [Publisher]

[32]. Minakshi M., Mitchell D.R., Munnangi A.R., Barlow A.J., Fichtner M. *Nanoscale*, 2018, **10**:13277 [Crossref], [Google Scholar], [Publisher]

[33]. Okoli N.L., Ezenwaka L.N., Okereke N.A., Ezenwa I.A., Nwori N.A. *Trends Sci*, 2022, **19**:5686 [Crossref], [Google Scholar], [Publisher]

[34]. Egwunyenga N., Onuabuchi V., Okoli N., Nwankwo I. *IRJMT*, 2021, **3**:1 [Crossref], [Google Scholar], [Publisher]

[35]. Egwunyenga N., Ezenwaka L., Ezenwa I., Okoli N. *MRX*, 2019, **6**:105921 [Crossref], [Google Scholar], [Publisher]

[36]. Augustine C., Nnabuchi M., Chikwenze R., Anyaegbunam F., Kalu P., Robert B., Nwosu C., Dike C., Taddy E. *MRX*, 2019, **6**:066416 [Crossref], [Google Scholar], [Publisher]

[37]. Saravanan V., Anusuya M., Ugwuoke C.O., Nwulu N., Ezema F.I. *Results Opt.*, 2023, **13**:100548 [Crossref], [Google Scholar], [Publisher]

[38]. Aboud A.A., Mukherjee A., Revaprasadu N., Mohamed A.N. *J. Mater. Res. Technol.*, 2019, **8**:2021 [Crossref], [Google Scholar], [Publisher]

[39]. Elekalachi C., Ezenwa I., Okereke A., Okoli N., Nwori A. *Nanoarchitectonics*, 2023, 26 [Crossref], [Google Scholar], [Publisher]

[40]. Nwori A.N., Ezenwaka L.N., Ottih I.E., Okereke N.A., Okoli N.L. *Trends Sci.*, 2022, **19**:5747 [Crossref], [Google Scholar], [Publisher]

[41]. Eze C., Ezenwa I., Okoli N., Elekalachi C., Okereke N. *J. Nano Mater. Sci. Res.*, 2023, **2**:123 [Crossref], [Google Scholar], [Publisher]

[42]. Onu C.P., Ekpunobi A.J., Okafor C.E., Ozobialu L.A. *Asian J. Res. Rev. Phy.*, 2023, **7**:17 [Crossref], [Google Scholar], [Publisher]

[43]. Nkele A.C., Nwankwo U., Alshoaibi A., Ezema F.I. *Results Opt.*, 2023, **13**:100521 [Crossref], [Google Scholar], [Publisher]

[44]. Contreras-Rodriguez R., Mendivil-Reynoso T., Landin I.O., Castillo S., Ochoa-Landín R. *ACS omega*, 2023, **8**:41411 [Crossref], [Google Scholar], [Publisher]

[45]. Whyte G., Awada C., Offor P., Whyte F., Kanoun M., Goumri-Said S., Alshoaibi A., Ekwealor A., Maaza M., Ezema F.I. *J. Alloys Compd.*, 2021, **855**:157324 [Crossref], [Google Scholar], [Publisher]

[46]. Ijeh R.O., Ugwuoke C.O., Ugwu E.B., Aisida S.O., Ezema F.I. *Ceram. Int.*, 2022, **48**:4686 [Crossref], [Google Scholar], [Publisher]

[47]. Tauc J., Grigorovici R., Vancu A. *physica status solidi (b)*, 1966, **15**:627 [Crossref], [Google Scholar], [Publisher]

[48]. Olubosede O., Faremi A.A., Owolabi F.M., Ajiboye E., Fateye J.O., Olanibi E.O. *FUOYE J. Eng. Technol.*, 2020, **5**:74 [Crossref], [Google Scholar], [Publisher]

[49]. Kumar K.D.A., Valanarasu S., Ganesh V., Shkir M., AlFaify S., Algarni H. *J. Mater. Res.*, 2018, **33**:1523 [Crossref], [Google Scholar], [Publisher]

[50]. Salim H., Olusola O., Ojo A., Urasov K., Dergacheva M., Dharmadasa I. *J. Mater. Sci. Mater. Electron.*, 2016, **27**:6786 [Crossref], [Google Scholar], [Publisher]

[51]. Ikhioya I.L., Aisida S.O., Ahmad I., Ezema F.I. *Chem. Phys. Impact*, 2023, **7**:100269 [Crossref], [Google Scholar], [Publisher]

[52]. Ikhioya I.L., Ugwuoke C.O., Obodo R.M., Okoli D., Eze C.U., Maaza M., Ezema F.I. *Appl. Surf. Sci. Adv.*, 2022, **9**:100232 [Crossref], [Google Scholar], [Publisher]

[53]. Okorieimoh C., Chime U., Nkele A.C., Nwanya A.C., Madiba I.G., Bashir A., Botha S., Asogwa P.U., Maaza M., Ezema F.I. *Superlattices Microstruct.*, 2019, **130**:321 [Crossref], [Google Scholar], [Publisher]

[54]. Ahmad I., Razzaq J., Ammara A., Kaleem F., Qamar M., Ilahi S., Ikhioya I.L. *Adv. J. Chem., Section A*, 2024, **7**: 110 [Crossref], [Google Scholar], [Publisher]

[55]. Samuel S.O., Lagbegha-ebi M.F., Ogherohwo E., Ikhioya I.L. *Results Opt.*, 2023, **13**:100518 [Crossref], [Google Scholar], [Publisher]

[56]. Saravanan V., Anusuya M., Nkele A.C., Ramachandran K., Shanthi A., Valsakumari M., Ezema F.I. *Appl. Surf. Sci. Adv.*, 2022, **11**:100294 [Crossref], [Google Scholar], [Publisher]

[57]. Boontan A., Barimah E.K., Steenson P., Jose G. *ACS Appl. Mater. Interfaces*, 2023, **15**:51606 [Crossref], [Google Scholar], [Publisher]

[58]. Awada C., Whyte G.M., Offor P.O., Whyte F.U., Kanoun M.B., Goumri-Said S., Alshoaibi A., Ekwealor A.B., Maaza M., Ezema F.I. *Nanomater.*, 2020, **10**:1557 [Crossref], [Google Scholar], [Publisher]